Available online at www.sciencedirect.com

ScienceDirect

Proceedings of the Combustion Institute 38 (2021) 3435–3443

Proceedings of the Combustion Institute

www.elsevier.com/locate/proci

Analysis of low-temperature chemistry in a turbulent swirling spray flame near lean blow-out

Danyal Mohaddes [a,*], Wenwen Xie [b], Matthias Ihme [a]

[a] *Department of Mechanical Engineering, Stanford University, Stanford, CA 94305, USA*
[b] *Center for Combustion Energy, Tsinghua University, Beijing 10084, China*

Received 8 November 2019; accepted 7 August 2020
Available online 14 October 2020

Abstract

An *n*-dodecane swirling spray flame from the Cambridge flame series is simulated using large-eddy simulation (LES) at conditions near the lean blow-out (LBO) limit. The focus of this study is to examine effects of low-temperature chemistry (LTC) and spray evaporation in turbulent spray combustion. To this end, a first simulation is performed using a finite rate chemistry model with a 55-species skeletal mechanism including LTC in a fully compressible Eulerian-Lagrangian formulation. A second simulation is performed using the same formulation, but with the LTC chemical sub-mechanism deactivated. The interactions of spray and gas-phase mixing and combustion are investigated through the consideration of mean and instantaneous LES results. Chemical explosive mode analysis (CEMA) is extended to account for droplet evaporation in the context of spray combustion, the results of which reveal that the flame is dominated by non-premixed combustion without significant auto-ignitive behavior. CEMA results further show that the effect of spray evaporation on the reaction is two-fold, namely to inhibit reaction near the injector through heat absorption, and to facilitate reaction further downstream by supplying fuel to the gas phase. Mixture fraction-conditioned analysis is then performed to evaluate the importance of LTC in the turbulent spray flame, showing its effect on heat release despite the flame not exhibiting auto-ignitive behavior. A polar mapping is proposed for analyzing the complex interplay of low and high temperature chemistry heat release. The results have consequences for numerical modeling of spray combustion systems where LTC effects are commonly neglected.
© 2020 The Combustion Institute. Published by Elsevier Inc. All rights reserved.

Keywords: Large-eddy simulation; Spray combustion; Chemical explosive mode analysis; Finite-rate chemistry; Low-temperature chemistry

1. Introduction

The study of turbulent spray combustion remains an active area of research due to its dominant role in aviation gas turbine engines [1]. Most gas turbine combustors achieve flame stabilization using inflow air swirl, whose associated flow reversal gives rise to a recirculation zone of hot combustion products.

As part of a broader experimental effort undertaken at the University of Cambridge to study swirl-stabilized combustion, a series of experiments with single-component liquid fuels at

---

[*] Corresponding author.
E-mail address: danmohad@stanford.edu
(D. Mohaddes).

https://doi.org/10.1016/j.proci.2020.08.030
1540-7489 © 2020 The Combustion Institute. Published by Elsevier Inc. All rights reserved.

ambient pressure were performed [2]. Experiments in this spray flame series have been simulated recently [3,4], largely focusing on *n*-heptane and ethanol fuels. The experiment in the series nearest LBO employing *n*-dodecane fuel is considered in this study using large-eddy simulation (LES) in conjunction with a finite-rate chemistry model.

Complex behavior arises in spray flames from the coupling of evaporation, combustion and the turbulent flow field, resulting in single and double flame structures across ranges of droplet diameters and strain rates. These effects have been demonstrated in steady laminar counterflow flames [5] and using direct numerical simulation (DNS) in turbulent counterflow configurations [6]. DNS studies of swirling spray combustion have shown the presence of multi-mode combustion regimes, including nonpremixed, partially premixed and premixed flames [7]. Further complexity arises due to low-temperature chemistry (LTC), which refers to the non-monotonic change in reactivity with reactant temperature of large hydrocarbons. Its manifestation as a two-stage ignition process in autoigniting fuel sprays has been well documented [8,9]. Recently, the coupling of LTC and spray evaporation has been demonstrated in a canonical one-dimensional steady laminar counterflow flame configuration [10], but its effects in steady turbulent spray combustion systems have been largely neglected [4,6,7,11]. While this work will focus on a steady swirl-stabilized turbulent spray configuration, a demonstration of some of the effects of the spray-chemistry coupling and LTC in the canonical configuration is provided as Supplemental Material.

The transition between low and high temperature oxidation in alkanes is driven primarily by the following elementary reactions [12]

$$\mathrm{R} + \mathrm{O_2} \rightleftharpoons \mathrm{ROO} \tag{I}$$

$$\mathrm{ROO} \rightleftharpoons \mathrm{QOOH} \tag{II}$$

$$\mathrm{ROO} \rightleftharpoons \mathrm{alkene} + \mathrm{HO_2} \tag{III}$$

where R is an alkyl radical formed by H-abstraction, ROO is an alkylperoxy radical, and QOOH is a hydroperoxyalkyl radical. At high temperatures, $\mathrm{I_f}$ is dominated by the high-temperature chemistry (HTC) pathway $\mathrm{R} \rightarrow \mathrm{alkene} + \mathrm{R}'$, where the subscripts f and b denote forward and backward reactions, respectively. At low temperatures, $\mathrm{I_f}$ becomes active and $\mathrm{II_f}$ dominates $\mathrm{III_f}$, whereby QOOH activates a low-temperature chain-branching pathway. At intermediate temperatures, $\mathrm{III_f}$ becomes active, but at such temperatures $\mathrm{HO_2}$ is largely stable and hence chain-terminating. This, and the endothermic dissociation of ROO in $\mathrm{I_b}$ with increasing temperature result in non-monotonic reactivity.

The objective of this study is to examine the effects of LTC and spray evaporation near LBO in a swirl-stabilized *n*-dodecane/air combustor. The remainder of the manuscript is structured as follows. The governing equations for gas and spray phases and related numerical methods are presented in Section 2, as are the modeling strategies for chemistry. The experimental configuration and related numerical setup are described in Section 3. Simulation results obtained from statistical analysis and chemical explosive mode analysis are discussed in Section 4. The manuscript closes with conclusions in Section 5.

2. Mathematical formulation

2.1. Gas-phase equations

An Eulerian-Lagrangian framework is employed in the context of LES to simulate spray combustion. The Favre-filtered governing equations for mass, momentum, total energy and species in the Eulerian gaseous phase are augmented with source terms arising from the Lagrangian spray phase as

$$D_t\bar{\rho} = -\bar{\rho}\nabla\cdot\tilde{\boldsymbol{u}} + \bar{\dot{S}}_\rho \tag{1a}$$

$$\bar{\rho}D_t\tilde{\boldsymbol{u}} = -\nabla\bar{p} + \nabla\cdot\bar{\boldsymbol{\tau}}_{\nu+t} + \bar{\dot{\boldsymbol{S}}}_{\boldsymbol{u}} \tag{1b}$$

$$\bar{\rho}D_t\tilde{e}_t = -\nabla\cdot(\bar{p}\tilde{\boldsymbol{u}}) + \nabla\cdot(\bar{\boldsymbol{\tau}}_{\nu+t}\cdot\tilde{\boldsymbol{u}}) - \nabla\cdot\bar{\boldsymbol{q}}_{\nu+t} + \bar{\dot{S}}_{e_t} \tag{1c}$$

$$\bar{\rho}D_t\tilde{Y}_k = -\nabla\cdot\bar{\boldsymbol{j}}_{k,\nu+t} + \bar{\dot{\omega}}_k + \bar{\dot{S}}_{Y_k} \tag{1d}$$

where $D_t = \partial_t + \tilde{\boldsymbol{u}}\cdot\nabla$ is the material derivative, ρ is the density, $\boldsymbol{u}$ is the velocity vector, p is the pressure, $\boldsymbol{\tau}$ is the viscous stress tensor, e_t is the specific total energy, $\boldsymbol{q}$ is the heat flux, Y_k is the species mass fraction, $\boldsymbol{j}_k$ is the species flux and $\dot{\omega}_k$ is the reaction source term, where the subscript k denotes the k-th species. Subscripts ν and t denote viscous and turbulent contributions, respectively. The interphase exchange terms $\dot{S}$ provide coupling from the spray phase to the gas phase. Subgrid-scale turbulence is modeled using the Vreman model [13] and turbulence-chemistry interactions are considered using the dynamic thickened-flame model [14] employing a maximum thickening factor of 3. The system is closed with the ideal gas equation of state.

2.2. Lagrangian spray particle approach

A Lagrangian spray-particle (LSP) method is employed for modeling the spray phase. The evolution of individual droplets is governed by the Lagrangian equations for droplet position, velocity, temperature and mass [15]

$$d_t\boldsymbol{x}_d = \boldsymbol{u}_d, \tag{2a}$$

$$d_t\boldsymbol{u}_d = \frac{f_1}{\tau_d}(\tilde{\boldsymbol{u}}(\boldsymbol{x}_d) - \boldsymbol{u}_d), \tag{2b}$$

$$d_t T_d = \frac{\mathrm{Nu}}{3\mathrm{Pr}_g}\frac{c_p}{c_l}\frac{f_2}{\tau_d}\left(\tilde{T}(\boldsymbol{x}_d) - T_d\right) + \frac{L_v}{c_l}\frac{\dot{m}_d}{m_d}, \quad (2c)$$

$$d_t m_d \equiv \dot{m}_d = -\frac{\mathrm{Sh}}{3\mathrm{Sc}_g}\frac{m_d}{\tau_d}H_M, \quad (2d)$$

where $\boldsymbol{x}_d$, $\boldsymbol{u}_d$, T_d, m_d and $\dot{m}_d$ are the droplet position, velocity, temperature, mass and mass evaporation rate, respectively, and $\tau_d \equiv \rho_l D_d^2/(18\mu_g)$ is the droplet relaxation time, where ρ_l is the liquid density, D_d is the droplet diameter, and μ_g is the gas-phase dynamic viscosity. $\tilde{T}(\boldsymbol{x}_d)$ and $\tilde{\boldsymbol{u}}(\boldsymbol{x}_d)$ denote the gas-phase temperature and velocity evaluated at the droplet position to achieve coupling of the gas phase to the spray phase. Pr_g and Sc_g are the gas-phase Prandtl and Schmidt numbers, c_p is the gas-phase heat capacity, and c_l and L_v are the liquid heat capacity and heat of vaporization. The coefficients Nu and Sh are the droplet Nusselt and Sherwood numbers from [16], and f_1 is the Stokes drag correction [15]. The evaporative heat transfer correction f_2 and mass transfer potential H_M are closed using a non-equilibrium Langmuir-Knudsen model (model M7 in [15]).

The use of the dynamic thickened-flame model as in Section 2.1 in conjunction with the LSP method poses a potential inconsistency for droplets which interact directly with thickened flame zones. Droplets in thickened regions will be exposed to elevated temperatures and hence undergo more rapid evaporation over a greater portion of their trajectory than had no thickening been applied. Hence, the right-hand-sides of Eqs. (2c) and (2d) are rescaled by the dynamic flame thickening factor as suggested in [17] to maintain consistency between the gas-phase LES and the spray-phase LSP approaches.

2.3. Finite rate chemistry

To study effects of spray evaporation and LTC on the flame structure, a 54-species skeletal mechanism for *n*-dodecane/air combustion [18] is employed. This mechanism explicitly accounts for LTC reactions following [19], allowing for the direct computation of LTC and HTC heat release rates $\dot{Q}_{LTC}$ and $\dot{Q}_{HTC}$ from $\dot{Q} = -\sum \dot{\xi}_i \Delta h_i$, where $\dot{\xi}_i$ and Δh_i are the net rate of chemical progress and the change in enthalpy for reaction *i*. Reactions I and II correspond to R252-R257 and R258-R259 in the mechanism, with III modelled by R260-R265 and the QOOH chain-branching pathway modelled by R266-R269. To enable direct comparison with a mechanism without LTC, a second mechanism was created by directly deactivating the LTC submechanism in [18] by removing reactions R252-R269. Both mechanisms were augmented with a sub-mechanism for the excited hydroxyl radical (OH*) [20] to allow for comparisons with experimental data. The modified mechanisms were verified using the original mechanism, see Supplemental Material for details.

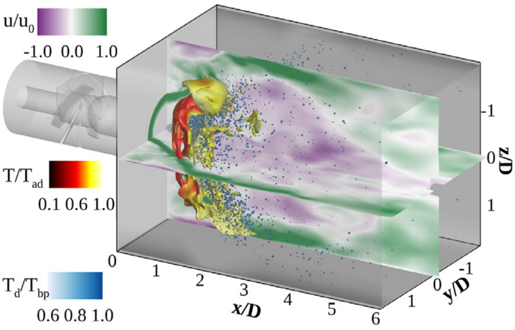

Fig. 1. Instantaneous visualization of flow field and computational domain for *n*-dodecane swirling spray flame. Isocontours of normalized axial velocity are plotted on inflow and center planes. Gas phase temperature isocontours normalized by the stoichiometric adiabatic flame temperature $T_{ad} = 2283$K are plotted on the $Y_{OH^*} = 10^{-12}$ isosurface. Fuel droplets are colored by their temperature normalized by the liquid boiling point $T_{bp} = 490$K.

2.4. Numerical methods

The unstructured, fully compressible finite-volume LES solver CharLES^x is used to solve the governing equations for gas and liquid phases. A sensor-based hybrid spatial discretization scheme is used for the Euler fluxes and the viscous fluxes are discretized using a nominally 4th-order scheme, as discussed in [21,22]. The computationally efficient second-order balanced operator-splitting algorithm of [23] for the temporal integration of the Navier-Stokes equations with stiff chemistry is augmented for spray combustion simulations with the Eulerian-Lagrangian approach by consistently incorporating LSP updates and inter-phase exchanges to ensure global conservation.

3. Experimental and computational setup

The configuration considered in this study is that of the Cambridge swirl-flame series for spray flames (case DD1S2) [2], and is shown in Fig. 1. Liquid *n*-dodecane fuel is injected from a hollow cone pressure atomizer with an angle of 60° at ambient temperature from the center of a bluff body of diameter $D = 25$mm into a chamber of square cross-section. The chamber is vented to an ambient pressure exhaust at a distance $L = 6D$ from the bluff body. Swirled, turbulent air at ambient temperature having bulk axial velocity $u_0 = 17.1$m/s and a swirl number of 1.23 enters the chamber from an annular inlet around the bluff body, giving a nominal flow-through time of $\tau_f = L/u_0 \approx 9$ms and global Bilger mixture fraction for the gas phase mixture of $Z_{g,glob} = 0.021$, corresponding to a fuel-lean global equivalence ratio of $\phi_{glob} = 0.32$. The value of u_0 considered corresponds to the nearest condition to LBO tested experimentally, at 85% of the blow-off velocity. The resultant flow field gives rise to an 'M'-shaped flame, comprising a primary inner and a secondary outer recirculation zone (IRZ and ORZ). The IRZ consists primarily of hot lean products, whereas the ORZ is primarily cold oxidizer. The configuration is such that the outer contour of the flame is stabilized on the shear layer formed by oxidizer inflow, whereas the inner contour of the flame is stabilized on the upstream side of the IRZ and interacts directly with the injected droplets, with some droplets penetrating the flame and entering the IRZ, as seen in Fig. 1. Experimental data [2] for the liquid phase are available for droplet Sauter mean diameter (SMD) as well as two components of mean and RMS droplet velocity from laser-Doppler/phase-Doppler anemometry (LDA/PDA). Mie scattering, OH planar laser induced fluorescence (OH-PLIF) and OH* chemiluminescence measurements are available for mean gas phase data.

The computational domain consists of the chamber as well as a large downstream section to represent exhaust to ambient pressure. To reduce computational cost, the swirling vanes and inflow annulus were pre-computed in a RANS simulation [24], from which the mean flow at the chamber inlet plane was imposed with synthetic turbulence having 20% intensity as an inflow boundary condition in the LES. The gas-phase inflow condition was validated in [24] for non-reacting and gas-phase reacting flow. The spray inflow boundary condition was prescribed by sampling droplet diameters from a Rosin-Rammler distribution with an SMD of $D_0 = 80$ µm and stretching factor $q = 3.0$, applying an injection velocity of 14m/s and a spreading factor of 10% about the nominal injection angle. Due to a lack of detailed characterization of the experimental spray boundary conditions, values of the injection velocity and spreading angle were chosen by attempting to match spray statistics at the first experimental measurement station as in [3].

The computational mesh consists of 6.5 million hexahedral cells primarily clustered from the inflow plane to a height of $2D$. The minimum and maximum spacings in the area of interest (from 0 to $1.6D$ both axially and radially) were 0.1mm and 0.55mm, resulting in a resolved turbulent kinetic energy fraction of 92% in the chamber based on the estimation method of [25]. Considering the premixed laminar flame thickness of a stoichiometric n-dodecane/air mixture at ambient conditions as a minimum reaction zone thickness, then after thickening as noted in Section 2.1 the present mesh yields a minimum of 6 grid points across the thickened reaction zone. The droplet to grid cell volume ratio was found to be below unity for all droplets. Considering a critical droplet Weber number for secondary droplet breakup of $We_c = 6$, the droplet diameters were sufficiently small to preclude any secondary breakup. Wall boundary conditions were prescribed as no-slip and isothermal at 298K.

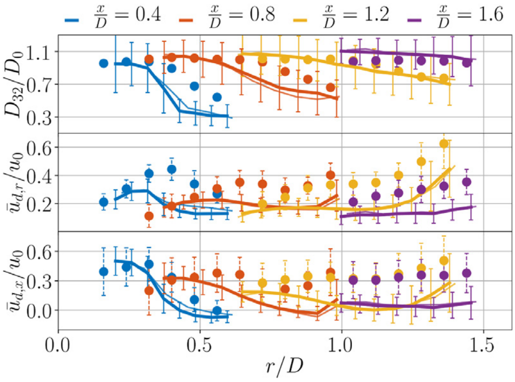

Fig. 2. Comparison of statistics for spray quantities. Symbols and lines indicate experimental and simulation data, respectively. Dashed and solid error bars show experimental and simulation RMS values, respectively. Heavy and light solid lines indicate simulation results with and without LTC, with RMS values plotted only for results with LTC.

4. Results and discussion

4.1. Physical space analysis

After allowing both simulations to reach steady-state over $3\tau_f$, flow field statistics were collected for both gas and spray phase quantities. Spray quantities are compared to experimental data in Fig. 2. As spray statistics are only indirectly influenced by the combustion chemistry, no significant difference between the two simulations is observed. From the figure, the spreading behavior of the hollow-cone injector is evident. Agreement for SMD is good at all axial measurement stations near the center of the spray cone. Over-prediction of the evaporation rate results in under-prediction of SMD at the radial extremities of the spray fan, but improves with increasing axial distance once most small droplets have evaporated. Axial and radial velocity components show reasonable agreement at the axial station nearest the injector, and are under-predicted with increasing axial and radial distance. Given that the droplet drag force is directly proportional to μ_g from Eq. 2b and that μ_g increases with temperature, this underprediction is a consequence of the overprediction of the flame

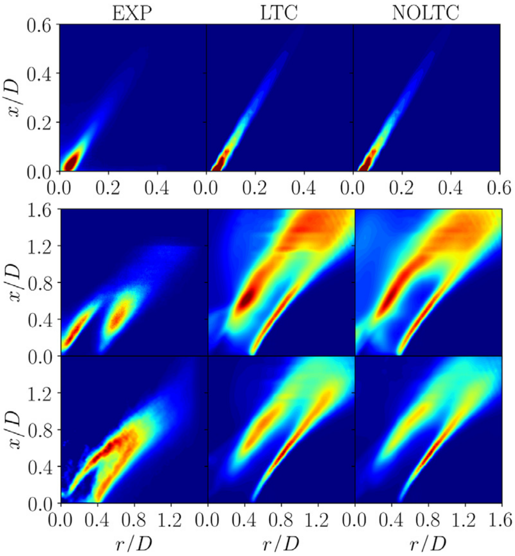

Fig. 3. Comparison of experiments to simulation results with and without LTC. Top row: Mean Mie scattering data and mean azimuthally-averaged α_l; middle row: Mean OH-PLIF data and mean azimuthally-averaged N_{OH}; bottom row: mean OH* chemiluminescence data and mean azimuthally-averaged Y_{OH^*}. Of these quantities, Y_{OH^*} in the inner flame region is most illustrative of the difference between simulations with and without LTC.

height and the associated larger region of high viscosity's impact on droplet drag forces.

Mean flow field data from both simulations is compared to measurements in Fig. 3. Mie scattering data is compared to liquid volume fraction α_l, and close agreement is achieved in both spray trajectory and the location of highest spray density, which occurs near the injector. As with the spray statistics in Fig. 2, significant differences due to combustion chemistry are not expected. OH-PLIF data is compared to OH number density N_{OH}, as number density is the first-order quantity determining LIF signal intensity [26], and inverse Abel transformed OH* chemiluminescence data is compared to results for Y_{OH^*}. Both simulations clearly recover the 'M'-flame structure, with an overprediction of the flame axial height. Overall, levels of agreement across the above experimental comparisons are reasonable and similar to those reported by other authors for the same spray flame configuration using *n*-heptane [4] and ethanol fuels [3].

Comparing the results with and without LTC, the most prominent difference is seen in the inner flame region, where spray-chemistry interaction is most significant, as will be discussed below in the context of Fig. 4. Considering the OH* results, the simulation with LTC correctly recovers a region of high OH* in the inner flame of comparable intensity to the outer flame, whereas the simulation without LTC does not. The same result can be seen in the OH fields, though it is less pronounced. This motivates the ensuing analysis of the simulation results with LTC to examine the effect of the LTC on the spray flame, and in particular the role of LTC in spray-chemistry interaction.

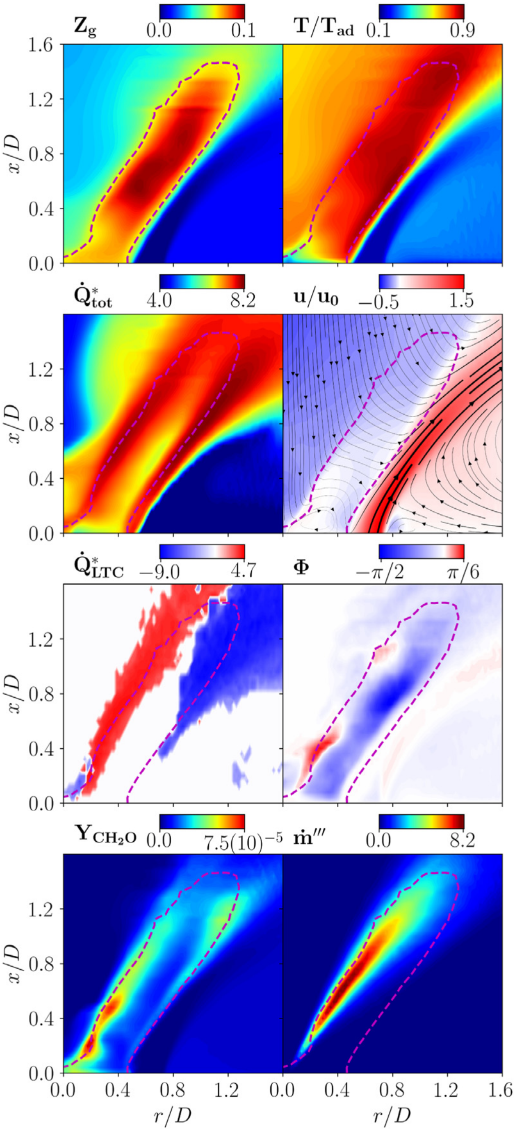

Fig. 4. Mean and azimuthally averaged CFD fields. Second row, right panel shows u/u_0 overlaid with mean azimuthally-averaged streamlines. Dashed magenta lines indicate the stoichiometric contour, and $\dot{m}'''$ has units of kg/m^3/s. In this work, the notations $a^* \equiv \mathrm{sign}(\mathcal{R}(a))\log_{10}(1+|\mathcal{R}(a)|)$ and $a^* \equiv \mathrm{sign}(a)\log_{10}(1+|a|)$ are used for the scaling of complex values and scalars, respectively.

The main features of the flow field and flame are shown in Fig. 4. Velocity streamlines show the flow reversal of the IRZ as well as the presence of a shear layer at the outer edge of this zone. The fuel injection trajectory, visible from α_l in Fig. 3, and the shear layer bound a fuel-rich zone in the IRZ, seen from the Z_g-field. The temperatures in this zone, seen from the T/T_{ad} field, are much higher than the rest of the IRZ and approach the adiabatic flame temperature. Consideration of the total heat release $\dot{Q}_{tot}$, where $\dot{Q}_{tot} = \dot{Q}_{LTC} + \dot{Q}_{HTC}$, shows that the highest heat release corresponds to the inner and outer parts of the stoichiometric isocontour. The 'M'-shaped flame is thus seen to arise from a double diffusion flame structure. The inner flame is stabilized within the IRZ, interacts significantly with the fuel spray and is oxidized by the hot products of fuel-lean combustion, while the outer flame is stabilized on the shear layer and is oxidized by fresh inflow air.

The interaction of the inner flame with the spray is demonstrated by the local mass vaporization rate $\dot{m}'''$. Injected droplets have initially low evaporation rates until they reach saturation due to heating from the gas phase, resulting in an induction region of low $\dot{m}'''$ near the injector. The vaporization rate increases along the injection trajectory, which corresponds closely to the inner stoichiometric contour, and reaches a maximum near $x/D = 0.8$. Formaldehyde mass fraction, a metastable species commonly used to identify LTC heat release [27], is seen to be highest in the inner flame within this induction region.

To quantify the relative contributions of LTC and HTC heat release rates to $\dot{Q}_{tot}$, a heat release phase angle is defined as

$$\Phi = \arctan\left(\dot{Q}_{LTC}/\dot{Q}_{HTC}\right) \tag{3}$$

using the signed arctangent function. Both $\dot{Q}_{LTC}$ and $\dot{Q}_{HTC}$ can be either exothermic or endothermic, resulting in four permissible quadrants for Φ. From Fig. 4 it is seen that the largest absolute values of $\dot{Q}_{LTC}$ are along the stoichiometric contour, exothermic on the inner flame and endothermic on the outer. However, the simultaneous consideration of Φ and $\dot{Q}_{LTC}$ shows that the relative contribution of LTC in the outer flame is negligible and that the absolute contribution in the fuel-rich region is negligible. LTC is most significant at the base of the inner flame, where it is exothermic.

Consideration of instantaneous flow field data provides insight into unsteady processes, shown in Fig. 5, particularly due to the non-monotonic dependence of LTC heat release on composition and temperature. The thermal evolution of the spray, including the induction region prior to droplet saturation noted above, is shown in the Z_g figure, where spray droplets within a cut plane are shown and colored by T_d/T_{bp}. The presence and spatial extent of the IRZ is seen from the contour of u/u_0, which is qualitatively similar to its mean profile seen in Fig. 4. Considering the instantaneous Z_g field, strong inhomogeneities are seen which are qualitatively dissimilar to the mean field and which reach levels up to twice as large as the maximum in the mean field. In these fuel-rich regions, $\dot{Q}_{tot}$ is seen to be endothermic. From the instantaneous Φ field it is clear that this endothermicity is attributable to high-temperature chemistry, since it corresponds to areas with $\Phi \approx \pm\pi$. The effect of the endothermic heat release on the flow field is seen in the instantaneous temperature. In most of the areas away from the injector and between the spray trajectory and the shear layer, the IRZ gas temperature is near T_{ad}. However, areas of high mixture fraction and strong endothermic heat release are seen to have substantially reduced gas temperatures. LTC heat release is seen to largely coincide spatially with droplet locations and is present in areas with both endothermic and exothermic total heat release. The structure of $\dot{Q}_{LTC}$ observed here will be addressed in Section 4.3.

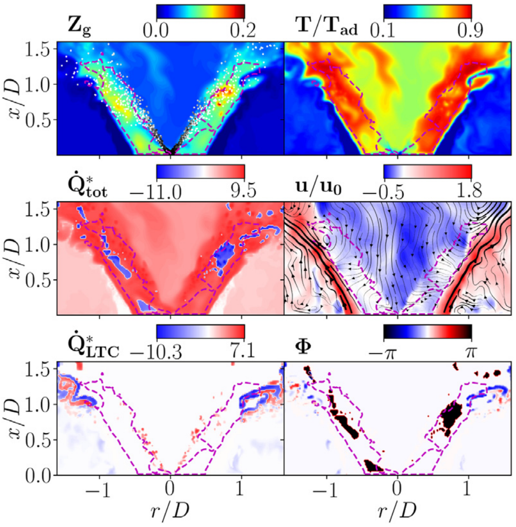

Fig. 5. Instantaneous flow-field data from LES. Top row, left panel shows Z_g overlaid with spray droplets colored by T_d/T_{bp}. Middle row, right panel shows u/u_0 overlaid with in-plane streamlines. Dashed magenta lines indicate the stoichiometric isocontour. The color map used for the phase angle Φ is cyclic: values near $-\pi$ and π are both rendered as black and indicate that endothermic HTC heat release is dominant.

4.2. Chemical explosive mode analysis

Chemical explosive mode analysis (CEMA) is an eigen-analysis of the spatiotemporally local fluid state vector $\boldsymbol{\varphi} = [\rho\boldsymbol{u}, \rho e_t, \rho\mathbf{Y}]^T$ for the identification of flame features [28] and the quantitative characterization of flow-chemistry coupling [29]. To identify combustion modes in the domain, particularly those of auto-ignition and non-premixed combustion, as well as to analyze the effect of the spray on reactivity, CEMA [30] is extended to the

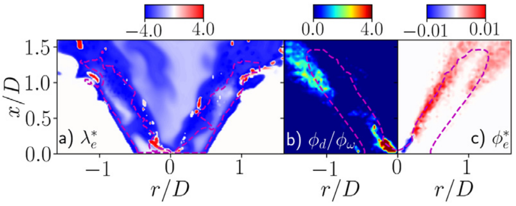

Fig. 6. Analysis of LES results using CEMA. (a) instantaneous λ_e^*; (b) mean azimuthally-averaged ϕ_d/ϕ_ω; (c) mean azimuthally-averaged ϕ_e^*. Dashed magenta lines indicate the stoichiometric isocontour.

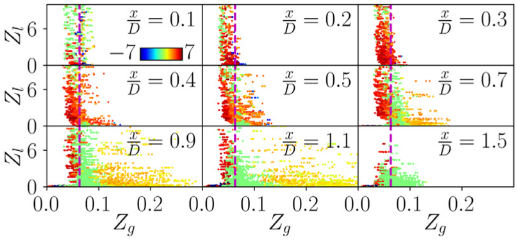

Fig. 7. $\dot{Q}_{LTC}^*$ scatter data on Z_l and Z_g as a function of axial distance. Values of $Z_l > 10$ were not plotted. Dashed magenta lines indicate $Z_g = Z_{st}$.

filtered equations of multiphase flow in the context of the dynamically thickened flame model. A detailed derivation is provided as Supplemental Material, but the key aspects are discussed below.

Eq. (1) may be re-written as $D_t\boldsymbol{\varphi} = \mathbf{g}_\omega(\boldsymbol{\varphi}) + \mathbf{g}_d + \mathbf{g}_e + \mathbf{g}_f$, where $\mathbf{g}_{\boldsymbol{\omega}}$, $\mathbf{g}_d$, $\mathbf{g}_e$ represent the filtered reaction source term, diffusion term and evaporation source term, respectively, and $\mathbf{g}_f$ denotes the other terms in Eq. (1). Applying the chain rule, the filtered equations are rewritten in terms of the chemical Jacobian $\mathbf{J} = \partial_{\boldsymbol{\varphi}}\mathbf{g}_\omega$ as

$$D_t\mathbf{g}_\omega = \mathbf{J} \cdot D_t\boldsymbol{\varphi} = \mathbf{J} \cdot \left[\mathbf{g}_\omega(\boldsymbol{\varphi}) + \mathbf{g}_d + \mathbf{g}_e + \mathbf{g}_f\right]. \quad (4)$$

CEMA identifies flame characteristics based on the eigen-analysis of $\mathbf{J}$. The primary chemical mode is described by the eigenvalue of $\mathbf{J}$ having the largest magnitude real part and its associated left eigenvector, denoted λ_e and $\mathbf{b}_e$, respectively. Defining $\phi = \mathbf{b}_e \cdot \mathbf{g}$, Eq. 4 is projected to the mode associated with λ_e and rearranged as $D_t\phi_\omega = \lambda_e\left(\phi_\omega + \phi_d + \phi_e + \phi_f\right) + D_t\mathbf{b}_e \cdot \mathbf{g}_\omega$, where ϕ_ω, ϕ_d and ϕ_e represent the projected chemical, diffusion and evaporation terms, and $D_t\mathbf{b}_e \cdot \mathbf{g}_{\boldsymbol{\omega}}$ was shown to be negligible [30]. CEMA thus provides diagnostic information of flame features through the consideration of the signed magnitudes of ϕ_i and λ_e. Chemical explosive modes (CEMs) are associated with $\mathcal{R}(\lambda_e > 0)$, and ratios between the projection terms reflect their relative importance in the combustion process.

Results from the CEMA flame analysis are shown in Fig. 6. Comparing Fig. 6a to Fig. 5 shows that instantaneously $\lambda_e < 0$ around most of the stoichiometric contour and zones of highest heat release. This shows that the flame is indeed in a non-premixed mode, with a small CEM zone with $\lambda_e > 0$ near the injector. From Fig. 6b, it is seen that $\phi_d/\phi_\omega > 1$ in the CEM zone, identifying this as an assisted-ignition mode where diffusion is dominant and promotes CEM.

The role of spray evaporation is analyzed from the averaged ϕ_e in Fig 6c. With increasing axial distance, ϕ_e is seen to change sign due to competition between two effects. Near the injector in the induction region discussed in Section 4.1, the spray tends to inhibit reaction progress through heat absorption, with low droplet evaporation rates prior to reaching saturation. As the evaporation rate increases, the endothermic effect of the vaporization process is overwhelmed by the resultant supply of fuel vapor to the reaction.

4.3. Composition space analysis

Spray evolution with axial distance is considered in gas-liquid composition space using instantaneous scatter data in Fig. 7. Near the injector and hence before significant evaporation, LTC heat release is small and a large range of liquid-to-gas mass ratio Z_l is present, where the presence of Z_g is due to recirculation. At axial locations up to $x/D \approx 0.5$, $\dot{Q}_{LTC} > 0$, as was seen in Fig. 5 from the apparent coincidence of locations with $\dot{Q}_{LTC} > 0$ with droplet positions. With increasing axial distance, higher values of Z_g are accessed as the spray interacts with the fuel-rich zone between the flame fronts. A regime of isothermal LTC develops on the rich side of Z_{st} and expands with axial distance, with the range of Z_l decreasing concurrently since by $x/D = 1.5$ most droplets have evaporated, as seen from α_l in Fig. 3.

Further analysis of the flow field is performed by considering scatter plots of instantaneous flow field data in Fig. 8. In Z_g space, temperature data shows significant variability. This is to be expected owing to the effects of turbulence as well as the non-adiabatic effects on the gas phase of spray evaporation and the combustor walls. The endothermic behavior of HTC is shown to be almost exclusively confined to fuel-rich regions with $Z_g > 0.09$. LTC is seen to have more complex behavior, being isothermal for much of the Z_g-space but with both significant endothermic and exothermic heat release for fuel-lean mixtures around $Z_g \approx 0.02$.

Considering $\dot{Q}_{LTC}$ in the context of the chemical description of LTC of Section 1, it can be seen that LTC heat release is confined to a narrow temperature window of $0.2 \lesssim T/T_{ad} \lesssim 0.5$. For $T/T_{ad} \gtrsim 0.5$, $\mathrm{I_f}$ is dominated by the HTC pathway, and for $T/T_{ad} \lesssim 0.2$ there is insufficient heat for LTC pathway activation. In the temperature range corresponding to non-monotonic changes

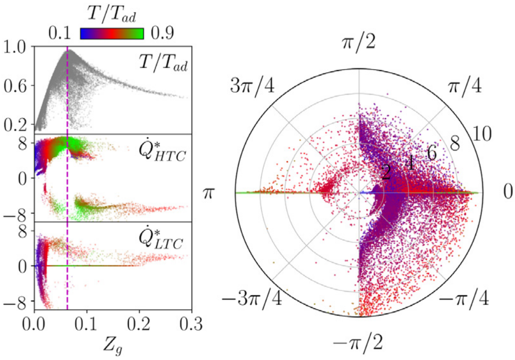

Fig. 8. Scatterplots of instantaneous LES data. Left: temperature and heat release rates in Z_g-space colored by T/T_{ad}; right: polar representation of heat release rate, with angle Φ and magnitude $\dot{Q}^*_{mag}$, colored by T/T_{ad}.

in reactivity for ambient pressure *n*-dodecane/air mixtures $0.3 \lesssim T/T_{ad} \lesssim 0.4$, $\dot{Q}_{LTC}$ exhibits bimodal behavior, a consequence of the strong sensitivity to temperature and composition in this regime where neither the forward nor backward reactions of I, II or III are dominant.

The importance of LTC in spray combustion can be shown by considering a polar representation of instantaneous heat release rate, with phase Φ and magnitude $\dot{Q}^*_{mag}$, where $\dot{Q}_{mag} = (\dot{Q}^2_{LTC} + \dot{Q}^2_{HTC})^{1/2}$. In this representation, a chemical mechanism which does not consider LTC will only access the horizontal line corresponding to $\Phi = 0$, $\Phi = \pm\pi$. The results of the present simulation show that the interplay of LTC and HTC heat release is rich and complex, with three of four potential heat release quadrants significantly represented in the spray combustor. The highest temperatures are clustered about the horizontal, where LTC was shown in the discussion above to be inert. In the two sectors $\Phi = [\pi/4, \pi/2]$ and $\Phi = [-\pi/4, -\pi/2]$ within the exothermic HTC regime, LTC is dominant. In the former case HTC heat release is augmented, and in the latter it is dominated, resulting in a net endothermic heat release. The LES results show that LTC heat release is present and significant for *n*-dodecane spray flames, and can both augment and compete with HTC effects.

5. Conclusions

Large-eddy simulations of an *n*-dodecane turbulent swirling spray flame were performed with and without LTC sub-mechanisms. Results showed good agreement with experiments, but results with LTC were more representative where spray-flame interactions were most significant. Gaseous and spray phase dynamics were analyzed in mean and instantaneous contexts. CEM analysis showed that the flame accesses multiple combustion regimes, highlighting the spatial distribution of the diminishing and augmenting effects of spray evaporation on reactivity. Heat release attributable to LTC was shown to be significant in the spray flame despite the flame being non-autoignitive, and should therefore be taken into account when selecting chemical mechanisms for future spray combustion simulations.

Declaration of Competing Interest

The authors declare that they have no known competing financial interests or personal relationships that could have appeared to influence the work reported in this paper.

Acknowledgments

Financial support from NAVAIR under contract number N68335-19-C-0177, The Boeing Company under grant number 134708 (IC2017-2182), and NASA with award number NNX15AV04A are gratefully acknowledged. The National Natural Science Foundation of China (grant no. 91841302) and the China Scholarship Council is acknowledged for support of the student exchange program. This research used resources of the National Energy Research Scientific Computing Center, a U.S. Department of Energy Office of Science User Facility operated under Contract no. DE-AC02-05CH11231.

Supplementary material

Supplementary material associated with this article can be found, in the online version, at doi:10.1016/j.proci.2020.08.030.

References

[1] A. Lefebvre, D. Ballal, *Gas Turbine Combustion*, CRC Press, 2010.
[2] R. Yuan, J. Kariuki, E. Mastorakos, *Int. J. Spray Combust. Spray Dyn.* 10 (3) (2018) 185–210, doi:10.1177/1756827718763559.
[3] A. Giusti, E. Mastorakos, *Proc. Combust. Inst.* 36 (2) (2017) 2625–2632, doi:10.1016/j.proci.2016.06.035.
[4] D. Paulhiac, B. Cuenot, E. Riber, L. Esclapez, S. Richard, *Combust. Flame* 212 (2020) 25–38, doi:10.1016/j.combustflame.2019.10.013.
[5] E. Gutheil, *Prog. Comp. Fluid Dyn.* 5 (7) (2005) 414, doi:10.1504/PCFD.2005.007428.
[6] A. Vié, B. Franzelli, Y. Gao, T. Lu, H. Wang, M. Ihme, *Proc. Combust. Inst.* 35 (2) (2015) 1675–1683, doi:10.1016/J.PROCI.2014.06.083.
[7] K. Luo, H. Pitsch, M. Pai, O. Desjardins, *Proc. Combust. Inst.* 33 (2) (2011) 2143–2152, doi:10.1016/j.proci.2010.06.077.

[8] X. Fu, S.K. Aggarwal, *Fuel* 144 (2015) 188–196, doi:10.1016/j.fuel.2014.12.059.
[9] P.B. Govindaraju, T. Jaravel, M. Ihme, *Proc. Combust. Inst.* 37 (3) (2019) 3295–3302, doi:10.1016/j.proci.2018.05.166.
[10] W. Xie, P.B. Govindaraju, Z. Ren, M. Ihme, *Submitted* (2020), doi:10.1016/j.proci.2020.06.274.
[11] L. Esclapez, P.C. Ma, E. Mayhew, R. Xu, S. Stouffer, T. Lee, H. Wang, M. Ihme, *Combust. Flame* 181 (2017) 82–99, doi:10.1016/j.combustflame.2017.02.035.
[12] H.J. Curran, *Proc. Combust. Inst.* 37 (1) (2019) 57–81, doi:10.1016/j.proci.2018.06.054.
[13] A.W. Vreman, *Phys. Fluids* 16 (10) (2004) 3670–3681, doi:10.1063/1.1785131.
[14] J.P. Légier, T. Poinsot, B. Varoquié, F. Lacas, D. Veynante, in: IUTAM Symposium on Turbulent Mixing and Combustion, Kluwer Academic Publishers, 2002, pp. 315–326, doi:10.1007/978-94-017-1998-8_27.
[15] R. Miller, K. Harstad, J. Bellan, *Int. J. Multiphase Flow* 24 (6) (1998) 1025–1055, doi:10.1016/S0301-9322(98)00028-7.
[16] W. Ranz, W. Marshall, *Chem. Eng. Prog.* 48 (3) (1952).
[17] F.L. Sacomano Filho, G. Kuenne, M. Chrigui, A. Sadiki, J. Janicka, *Combust. Flame* 184 (2017) 68–89, doi:10.1016/j.combustflame.2017.05.031.
[18] T. Yao, Y. Pei, B.-J. Zhong, S. Som, T. Lu, K.H. Luo, *Fuel* 191 (2017) 339–349, doi:10.1016/j.fuel.2016.11.083.
[19] G. Bikas, N. Peters, *Combust. Flame* 126 (2001) 1456–1475, doi:10.1016/S0010-2180(01)00254-1.
[20] J.M. Hall, E.L. Petersen, *Int. J. Chem. Kinet.* 38 (12) (2006) 714–724, doi:10.1002/kin.20196.
[21] Y. Khalighi, J.W. Nichols, S.K. Lele, F. Ham, P. Moin, *AIAA Paper* (2011) 2011–2886, doi:10.2514/6.2011-2886.
[22] P.C. Ma, Y. Lv, M. Ihme, *J. Comput. Phys.* 340 (2017) 330–357, doi:10.1016/j.jcp.2017.03.022.
[23] H. Wu, P.C. Ma, M. Ihme, *Comput. Phys. Commun.* 243 (2019) 81–96, doi:10.1016/J.CPC.2019.04.016.
[24] P.C. Ma, H. Wu, J.W. Labahn, T. Jaravel, M. Ihme, *Proc. Combust. Inst.* 37 (2019) 5073–5082, doi:10.1016/j.proci.2018.06.066.
[25] S. Pope, *Turbulent Flows*, Cambridge University Press, 2000.
[26] S. Popp, F. Hunger, S. Hartl, D. Messig, B. Coriton, J.H. Frank, F. Fuest, C. Hasse, *Combust. Flame* 162 (8) (2015) 3016–3029, doi:10.1016/j.combustflame.2015.05.004.
[27] S.A. Skeen, J. Manin, L.M. Pickett, *Proc. Combust. Inst.* 35 (3) (2015) 3167–3174, doi:10.1016/j.proci.2014.06.040.
[28] T.F. Lu, C.S. Yoo, J.H. Chen, C.K. Law, *J. Fluid Mech.* 652 (2010) 45–64, doi:10.1017/s002211201000039x.
[29] C. Xu, J.-W. Park, C.S. Yoo, J.H. Chen, T. Lu, *Proc. Combust. Inst.* 37 (2) (2019) 2407–2415, doi:10.1016/j.proci.2018.07.069.
[30] W. Wu, Y. Piao, Q. Xie, Z. Ren, *AIAA J.* 57 (4) (2019) 1355–1363, doi:10.2514/1.J057994.